

# On modeling and measuring viscoelasticity with dynamic Atomic Force Microscopy

Per-Anders Thorén,<sup>1,\*</sup> Riccardo Borgani,<sup>1</sup> Daniel Forchheimer,<sup>1</sup> Illia Dobryden,<sup>2</sup> Per M. Claesson,<sup>2</sup>  
Hailu G. Kassa,<sup>3</sup> Philippe Leclère,<sup>3</sup> Yifan Wang,<sup>4</sup> Heinrich M. Jaeger,<sup>4</sup> and David B. Haviland<sup>1</sup>

<sup>1</sup>*KTH Royal Institute of Technology, Nanostructure Physics, Albanova, SE-10791 Stockholm, Sweden*

<sup>2</sup>*KTH Royal Institute of Technology, School of Chemical Science and Engineering, Department of Chemistry, Surface and Corrosion Science, Drottning Kristinas väg 51, SE-100 44 Stockholm, Sweden*

<sup>3</sup>*Laboratory for Chemistry of Novel Materials, Center for Innovation and Research in Materials and Polymers, University of Mons (UMONS), Place du Parc 20, B-7000 Mons, Belgium*

<sup>4</sup>*James Franck Institute, University of Chicago, 929 East 57th St., Chicago, IL 60637, USA*

The interaction between a rapidly oscillating atomic force microscope (AFM) tip and a soft material surface is described using both elastic and viscous forces with a moving surface model. We derive the simplest form of this model, motivating it as a way to capture the impact dynamics of the tip and sample with an interaction consisting of two components: interfacial or surface force, and bulk or volumetric force. We examine analytic solutions to our piece-wise linear model in some special cases. Numerical simulation is used to fit the model to experimental data and excellent agreement is found with a variety of different samples. The model parameters form a dimensionless impact-rheology factor, giving a quantitative physical characterization of a viscoelastic surface which is apparently independent of the AFM probe.

## I. INTRODUCTION

An increasingly important application of the Atomic Force Microscope (AFM) is characterization of the viscoelastic response of soft materials and interfaces, such as cells membranes and tendons[1–4], polymer blends and composites [5–11], the liquid-gas[12] and liquid-solid [13] interfaces, and suspended membranes [14]. The present trend toward higher scanning speeds [15, 16] and higher resolution mechanical property mapping [17, 18] necessitates shorter time spent at each pixel of the scan, and therefore more rapid motion of the tip. With higher tip velocity the viscous contribution to the total force increases, requiring a dynamic force measurement method that can distinguish viscous from elastic force. Translating the measured forces to material properties also requires a model that captures the dynamics of both tip and sample. Such a viscoelastic model of AFM contact forces must look beyond bulk rheology to also include the rheology of the interface[19].

When a rigid AFM tip impinges a soft material surface it experiences different types of force: elastic force associated with strain in the volume of the material, surface force associated with the formation and changing curvature of the contacting interface, and viscous force associated with the rate of change of strain and curvature. These sample deformations occur at the nanometer scale in the AFM contact, where the surface-to-volume ratio is much larger than that of macroscopic contacts. We therefore expect surface forces to play a more important role in AFM.

Measuring viscoelastic forces with the AFM requires analysis of the tip and sample as a nonlinear dynamical

system. The AFM tip oscillating in and out of contact with the sample is a nanometer-scale example of a broader class of dynamical systems known as impact oscillators. These are often modeled with piece-wise non-smooth impact forces that produce interesting bifurcations [20]. The large quality factor  $Q$  of the cantilever resonance ensures the inertial and linear restoring forces of the cantilever body dominate the system dynamics. However, with the help of lockin measurement techniques one can observe signals due to the much-smaller impact forces which weakly perturb the harmonic motion of the cantilever. Here we use a recently developed multifrequency lockin method, where many Fourier components of the nonlinear tip-sample force are detected near resonance [21], providing much more information about the impact forces.

Tip-surface force in AFM is often described in terms of contact mechanics using the Hertz model [22], where elastic compression gives rise to a conservative repulsive force that does not dissipate energy in the oscillation cycle. A viscoelastic version of the Hertz model has been studied in the context of two-body collisions, where impact forces can be calculated in the center-of-mass reference frame [23]. With the center-of-mass in the laboratory frame, defined as the inertial reference frame where the bulk of the sample is at rest (sample mass  $\gg$  cantilever mass), the viscoelastic Hertzian model reduces to a Kelvin-Voigt expression for the tip-sample force, where dissipation is introduced as a viscous damping function that depends on tip position in the laboratory frame,  $F_{TS} = F_{con}(z) + \dot{z}\eta(z)$ . Other models of sample viscoelasticity modify contact mechanics using a creep-compliance picture, where the elastic modulus is time-dependant and force is determined by integrating over the deformation history [1–3]. Sample deformation in three dimensions can be modelled using finite elements of linear [24] or nonlinear force-displacement relations to account for an

---

\* pathoren@kth.se

attractive tip-sample force [25].

In contrast to these bulk viscoelastic models, tip-sample force in AFM may also be understood to result from purely interfacial phenomena. The change in interfacial energy upon contact is often called the work of adhesion, or in the context of wetting phenomena, the spreading parameter [26]  $W = (\gamma_T + \gamma_S) - \gamma_{TS}$ . Here the energies per unit area of the tip (sample)  $\gamma_{T(S)}$  and tip-sample interface  $\gamma_{TS}$ , are typically such that  $W > 0$ , resulting in adhesion, or attractive force upon contact. The role of surface energy in contact mechanics was originally discussed by Johnson, Kendal and Roberts (JKR) [27]. The JKR model has been shown to break down when the contact radius of curvature  $R$  is small in comparison with the elastocapillary length,  $L = \Upsilon/E$ , where  $\Upsilon$  is the surface stress and  $E$  is the Young's modulus of the sample bulk [28, 29]. For a soft material  $E \sim 3$  MPa forming a contact with relatively low interfacial energy  $\gamma_{TS} \sim 30$  mN/m and no additional surface stress (in which case  $\Upsilon = \gamma_{TS}$ ), we find  $L \sim 10$  nm, the typical radius of an AFM tip. Thus, even for moderately soft materials, the AFM impact should resemble a liquid-like sample wetting and forming a meniscus around the tip, as opposed to the tip compressing an elastic solid.

From the considerations given above it is clear that a first principles approach to modeling AFM contact dynamics is non-trivial, requiring many model parameters and degrees of freedom. Unfortunately, connecting such models to experimental AFM data is difficult because the AFM typically measures the dynamics of only one degree of freedom, the vertical deflection of the cantilever from its equilibrium position  $d(t)$ . It is therefore well-motivated to formulate reduced models which approximate the tip-sample collision dynamics. Such models usually assume that the interaction force can be written  $F_{TS}(z, \dot{z})$ , where  $z(t) = h + d(t)$  is the vertical position of the tip and  $h$  is the static probe height in the laboratory frame [see Fig. 1(a)]. This approach neglects the fact that the sample itself also has dynamics which is clearly important for a complete understanding.

Here we reduce the complicated three-dimensional dynamics of the sample to a simplified one-dimensional dynamics in terms of a single degree of freedom  $z_s(t)$ , describing the instantaneous vertical position of the surface in the laboratory frame. The interaction between the tip and the surface is then considered to be a function of the tip-sample separation  $s = z - z_s$ . This type of model was introduced in the context of AFM by Cantrell and Cantrell [30] and a variation of the model was compared with experiments in our previous publication [31]. Here we give a simplified version of the model, retaining only its essential features. The simple model allows us to develop intuition by considering analytic solutions in some limiting cases. We simulate the simplified model and introduce numerical optimization to find the parameters of the model which best fit experimental data. We close with a general discussion, introducing dimensionless ratios of model parameters which could serve as use-

ful quantities for nano-scale mechanical characterization of surfaces.

## II. THE MOVING SURFACE MODEL

All coordinates are defined in Fig. 1(a). An essential feature of any model describing dynamic AFM in air is a large force gradient  $\frac{d}{dz}F_{TS}(s, \dot{s})$  localized near the point of contact  $s = z - z_s = 0$ . This rapid change of force is responsible for the jump-to-contact and pull-off hysteresis seen in nearly all "force curves", or quasi-static measurements of  $d(h)$ . In dynamic AFM, when the tip is oscillating in and out of contact with the surface, the amplitude of oscillation is typically much larger than the range of this localized interaction. We may therefore approximate this region of large interaction gradient as an adhesion force which instantly turns on and off when crossing the point of contact. Figure 1b shows a piecewise linear (PWL) force model described by the following equations,

$$F_{TS}(s, \dot{s}) = \begin{cases} 0 & \text{if } s > 0 \\ -F_{ad} - k_v s - \eta_v \dot{s} & \text{if } s \leq 0 \end{cases} \quad (1)$$

The interaction force is zero when the tip is out of contact,  $s > 0$ . When in contact,  $s \leq 0$ , the adhesion force  $F_{ad}$  correspond to a lowering of the total interfacial energy. Adhesion is counteracted by a repulsive force linear in  $s$  as the tip penetrates below the surface, where the stiffness  $k_v$  describes elastic compression of the bulk in a local volume around the tip. We also include the possibility of a viscous force via the damping coefficient  $\eta_v$ , associated with material flow in this local volume.

The interaction force couples the dynamics of the cantilever's flexural eigenmode to the dynamics of the viscoelastic surface, described by the following set of equations.

$$m\ddot{d} + \eta\dot{d} + kd = F_{TS}(s, \dot{s}) + F_{drive}(t) \quad (2a)$$

$$\eta_s \dot{d}_s + k_s d_s = -F_{TS}(s, \dot{s}) \quad (2b)$$

Here  $d_s = z_s - z_0$  is the deflection of the surface from its equilibrium position  $z_0$  and  $F_{drive}(t)$  is the drive force.

The free motion of the tip is given by eq. (2a) with  $F_{TS} = 0$ , describing a driven damped simple harmonic oscillator. This model is valid in a narrow frequency band around a high quality factor resonance of the cantilever. The three mode parameters: stiffness  $k$ , resonant frequency  $\omega_0 = \sqrt{k/m}$  and dimensionless quality factor  $Q = \omega_0\tau = \sqrt{\eta^2/mk}$ , are independently determined using a calibration procedure (see Methods). The relaxation time or damping time  $\tau = \eta/k$  is the delay between applied force and cantilever response, resulting from the interaction of the cantilever body with its surrounding medium.

The free motion of the surface is described by eq. (2b) with  $F_{TS} = 0$ . Note that eq. (2b) does not have an

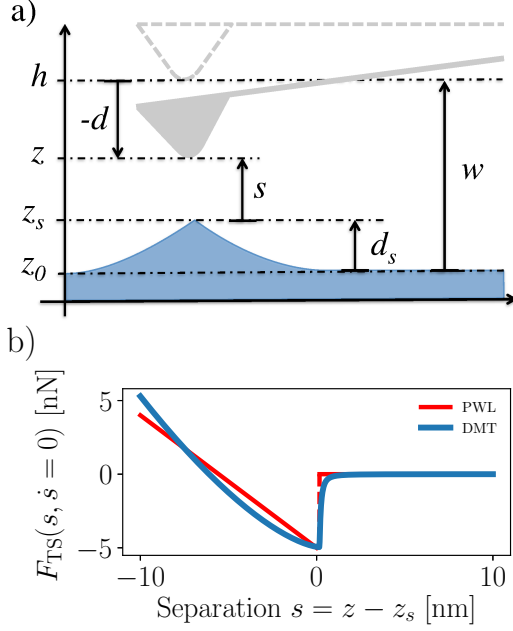


FIG. 1. **The moving surface model.** (a) Sketch, not to scale, defining the coordinates. The cantilever restoring force depends on the cantilever deflection  $d = z - h$ , measured by the AFM. The model introduces forces that depend on surface deflection  $d_s = z_s - z_0$  and the tip-surface separation  $s = z - z_s$ . Forces are balanced in the inertial reference frame where the cantilever has a fixed working distance to the sample  $w = h - z_0$ . (b) The piece-wise linear (PWL) interaction force plotted together with a calculated DMT model frequently used in AFM [32]. The parameters for the DMT model are: Reduced modulus  $E^* = 100$  MPa, Hamaker constant  $H = 8 \times 10^{-20}$  J, tip radius  $R = 10$  nm, inter-molecular spacing  $a_0 = 0.16$  nm. Parameters for the PWL model are:  $F_{ad} = 5$  nN,  $k_v = 0.9$  N/m. The range of separation shown is that typically covered by the cantilever oscillation for dynamic AFM on soft materials.

inertial term corresponding to force arising from acceleration of the sample mass. Neglecting sample mass is valid when deformation occurs only in a local volume around the tip, however inertial forces may arise if the cantilever excites standing surface waves [31]. Thus the model effectively puts the center-of-mass at the equilibrium position of the tip, which we treat as fixed in the laboratory frame. We therefore neglect the very small amplitude base motion needed to inertially actuate the high Q resonance [33], as well as any forces arising from rapid changes of the probe height (*e.g.* large  $\dot{h}$  or  $\ddot{h}$  due to over-active surface-tracking feedback).

We can develop intuition for the sample dynamics by considering what happens when the tip is held rigidly fixed in the laboratory frame (*i.e.* not connected to a flexible cantilever) at the height of the unperturbed surface. As the tip just touches the surface from above (see Fig. 2(a), the case  $s = 0$  in eq. (1) together with the

condition  $z = z_0$ , or equivalently  $s = -d_s$  in eq. (2b), gives

$$(\eta_s + \eta_v)\dot{d}_s + (k_s + k_v)d_s = F_{ad}. \quad (3)$$

Solving this equation we find that upon contact, the adhesion force lifts the surface

$$d_s(t) = \delta(1 - e^{-t/\tau_c}) \quad (4)$$

forming a meniscus with asymptotic height,

$$\delta = F_{ad}/(k_v + k_s). \quad (5)$$

in a characteristic contact formation time,

$$\tau_c = \frac{\eta_v + \eta_s}{k_v + k_s}. \quad (6)$$

Similarly, when the tip just separates from the lifted surface, eq. (1) for the case  $s > 0$  and eq. (2b) give,

$$\eta_s\dot{d}_s + k_s d_s = 0. \quad (7)$$

describing free relaxation of the surface to its equilibrium position in a characteristic time

$$\tau_s = \eta_s/k_s. \quad (8)$$

The contact formation and free relaxation dynamics are depicted in Fig. 2. We may also define the time constant

$$\tau_v = \frac{\eta_v}{k_v}, \quad (9)$$

associated with penetration of the tip and volumetric compression of the sample.

The model behaves as we would intuitively expect for an interaction consisting of two opposing forces: attractive surface force resulting from minimization of interfacial energy, and repulsive volumetric force resulting from compressive stress in the bulk. The stiffness parameter  $k_s$ , responsible for relaxation of the sample to equilibrium, includes both surface and bulk force with their relative contribution depending on the size of the deformation in relation to the elastocapillary length. The parameter  $k_v$  on the other hand describes elastic compression of the bulk. Nevertheless, a liquid-like interaction is described by  $K \equiv k_s/k_v \gg 1$ , in which case the meniscus lifts to a maximum height,

$$\delta \simeq \delta_0 \equiv F_{ad}/k_s \quad (10)$$

A solid-like interaction is described by the opposite limit  $K \ll 1$ , in which case  $\delta \ll \delta_0$  as capillary adhesion is counteracted by compressive stress in the contact volume.

The time constants  $\tau_c$ ,  $\tau_s$  and  $\tau_v$  represent ratios of viscous to elastic force constants of the model. The dynamics of both the tip and the sample depend on these characteristic times scales and their relation to time spent in and out of contact during a single oscillation cycle,

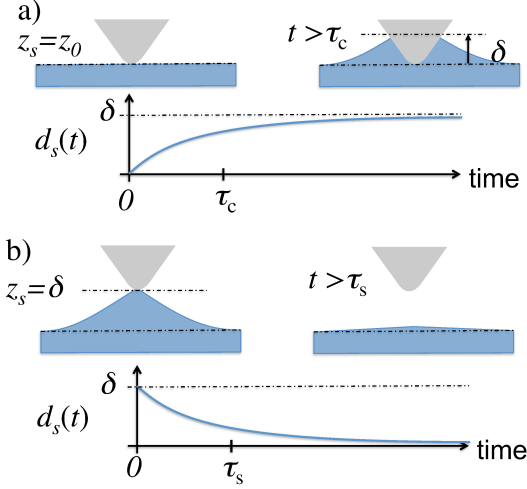


FIG. 2. **Contact formation and free relaxation.** (a) At  $t = 0$  a tip rigidly fixed in the laboratory frame meets the surface. The adhesion force turns on and the surface lifts by an amount  $\delta$ , forming the contact in a characteristic time  $\tau_c$ . (b) At  $t = 0$  the tip separates from the lifted surface. The surface relaxes to its equilibrium position in the characteristic time  $\tau_s$ .

where the latter is set by the frequency of cantilever oscillation, the amplitude of motion and working distance to the surface  $w = h - z_0$ . When the contact formation time  $\tau_c$  is larger than the time spent in contact, the surface can not fully deform to achieve contact equilibrium. When the free relaxation time  $\tau_s$  is large compared to time spent out of contact, the surface can not relax to its equilibrium position before the next tap of the tip. Repeated taps by the tip result in a steady-state dynamics characterized by a time-average up-lifted or indented position of the surface.

In the following section we demonstrate this behavior of the model and correlate it with data from experiments. We show that this simple model explains the experimental data remarkably well for a variety of different soft materials. Fitting the model to experimental data we extract the model parameters which characterize the material and its surface. We then comment on how these parameters may be useful for a general, quantitative method of characterization for viscoelastic samples with AFM.

### III. COMPARISON WITH EXPERIMENT

We have validated the model by fitting it to data collected on several different samples. Figure 3 show scanned images of four samples discussed below. To display the results of both experiment and theory, we show dynamic force quadrature curves using a technique called Intermodulation AFM (ImAFM) [21]. Force quadratures have been introduced in previous publications [34, 35] but

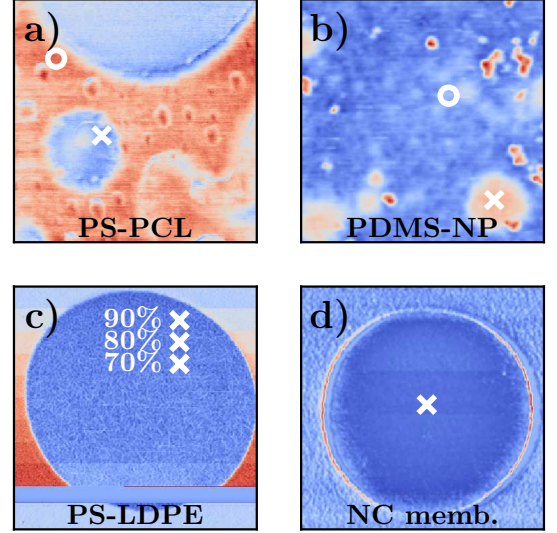


FIG. 3. **Samples analyzed in this paper.** (a) Scan size  $0.8 \mu\text{m}$ . Domains of Polycaprolactone (PCL, blue) in Polystyrene (PS, red). Pixels marked with  $\circ$  and  $\times$  are analyzed in Fig. 4. (b) Scan size  $1 \mu\text{m}$ . Polydimethylsiloxane (PDMS, blue) with clusters of hydrophobic silica nanoparticles (NP, red). Pixels marked with  $\circ$  and  $\times$  are analyzed in Fig. 5. (c) Scan size  $1.5 \mu\text{m}$ . A setpoint study on a domain of low density polyethylene (LDPE, blue) in PS. Pixels marked with  $\times$  are analyzed in Figs. 6, S1 and S2, at the setpoint values shown. (d) Scan size  $3 \mu\text{m}$ . A suspended membrane of Au nanoparticles bound together in a monolayer by organic ligands. A pixel at the center of the membrane (approximately marked with  $\times$ ) is analyzed in Fig. 7.

they are rather unfamiliar to the majority of AFM scientists so we briefly describe them here. Unlike the more familiar "force curves", they do not display the instantaneous force on the tip as a function of tip position, *i.e.*  $F_{\text{TS}}(z)$  measured at some constant value of  $\dot{h}$ . Rather, force quadratures represent integrals of force over single oscillation cycles, making them the natural force curves of dynamic AFM.

The large stored energy in the free cantilever oscillation ensures that the engaged motion will be very nearly harmonic and therefore well-described as oscillation at a fixed 'carrier' frequency  $\bar{\omega} \simeq \omega_0$ , with a slowly-modulated amplitude and phase. In the frequency domain this corresponds to response concentrated in a narrow-band around resonance. The force quadratures represent the Fourier components of the tip-sample force at this carrier frequency, but measured in a "rotating frame" such that

the cantilever motion always has zero phase.

$$d(t) = h + A \cos \bar{\omega} t \quad (11a)$$

$$F_I(A) = \int_0^T F_{TS}(t) \cos(\bar{\omega} t) dt \quad (11b)$$

$$F_Q(A) = \int_0^T F_{TS}(t) \sin(\bar{\omega} t) dt \quad (11c)$$

Thus  $F_I$  is the Fourier component which is in-phase with the motion, and  $F_Q$  quadrature to the motion, or in-phase with the velocity. The former represents a conservative force (*i.e.* energy which is recovered in the oscillation cycle), and the latter represents a dissipative force (*i.e.* energy lost in the cycle).

When the tip is tapping on the sample, large Fourier components of the tip-sample force also exist at frequencies far above resonance, but these induce only very weak cantilever response, well below the detection noise floor, due to the high-Q resonance of the cantilever. Thus, we can not determine the instantaneous force at any given time in the cycle. However, we can determine the integrated force over single cycles with very good signal-to-noise ratio, using the multifrequency lockin technique embodied in ImAFM. The method allows one to make the transformation to the rotating frame, enabling determination of the force quadratures as functions of the oscillation amplitude  $A$ . Two curves  $F_I(A)$  and  $F_Q(A)$  are found by direct transformation of the multi-frequency response, requiring only the calibrated linear response function of the cantilever eigenmode. No assumptions are made regarding the specific nature of the tip-sample interaction. This transformation is quite efficient computationally, allowing for immediate examination of the force quadrature curves at individual pixels, while scanning.

Figure 4 shows force quadrature curves taken at two different points on a blend of polystyrene (PS) and polycaprolactone (PCL), shown in Fig. 3(a). The force quadratures on the softer PCL (bulk modulus ca. 300 MPa) show larger magnitude of the dissipative force  $F_Q$  and a conservative force which is dominantly attractive,  $F_I > 0$ , even at the highest amplitude. To fit the theory to the experimental data, we simulate the model dynamics by numerical integration of the equations of motion eq. (2a) and eq. (2b), adjusting the parameters of the model to find a best fit. Details of this procedure are given in the Methods section.

On the soft PCL we find an excellent fit and simulation shows that the adhesive force causes the surface to lift about 15 nm on average [Fig. 4(d)]. The zoom of individual oscillation cycles [Fig. 4(c)] shows that upon impact the tip penetrates as much as  $\sim 20$  nm below the lifted surface. After separation on the upward trajectory of the cantilever, the surface does not have time to fully relax to its equilibrium position before the next impact. This slow relaxation of the surface gives rise to the hysteresis observed in the  $F_I(A)$  and  $F_Q(A)$  curves: The amplitude at which the surface is initially up-lifted

(sharp up-turn in  $F_I(A)$ ), is larger than the amplitude where the oscillating tip fully releases the surface (sharp down-turn in  $F_I(A)$ ).

We compare the behavior on the softer PCL with that on the stiffer PS domain (bulk modulus ca. 3 GPa). On PS we find that the conservative force quadrature  $F_I$  becomes dominantly repulsive ( $F_I < 0$ ) at large amplitude, and we see a smaller magnitude of the dissipative force  $F_Q$ . Simulations show that the tip penetrates as much as 10 nm below the surface, but the surface lifts only slightly and quickly relaxes to its equilibrium position before the next impact. For increasing  $A$  the simulation captures the shape and magnitude of both  $F_I(A)$  and  $F_Q(A)$ . However for decreasing  $A$  we find that the simulation does not reproduce the hysteresis observed in the experiment. A different interaction function  $F_{TS}(s)$  could improve the quality of the fit, but at the expense of introducing additional model parameters. In our experience, the simplified model presented herein often does not capture hysteresis observed together with  $F_I < 0$ , but it nearly always captures hysteresis when  $F_I > 0$ .

In Fig. 5 we show an additional example of model fitting at two locations on a sample consisting of PDMS mixed with hydrophobic silica nanoparticles, shown in Fig. 3b. This soft sample had faster free relaxation (smaller  $\tau_s$ ) such that no hysteresis is seen in the force quadratures. Fitting to the model shows that there is rather large amplitude surface motion when tapping on the PDMS matrix. When tapping on a region with dispersed nanoparticles, the model shows a much slower surface and very low amplitude surface motion, but equally deep penetration.

We also investigated how the fitted model parameters depend on a change of tip and cantilever oscillation frequency. Using three standard tapping mode cantilevers with calibrated parameters given in Table I, we studied a well-known soft material consisting of micron size domains of low-density polyethylene (LDPE, bulk modulus ca. 100 MPa) in a matrix of PS [37], as shown in Fig. 3c. The cantilever resonant frequencies and mode stiffnesses span one order of magnitude. In order to make a reasonable comparison we adjusted the excitation to keep the amplitude of free motion  $A_{\text{free}}$  such that stored energy in the free oscillation  $E_{\text{free}} = \frac{1}{2} k A_{\text{free}}^2$  is approximately the same for each cantilever. Table I also shows the best-fit parameters of the moving surface model.

For each cantilever we also study how the force quadrature curves change as we vary the working distance,  $w = h - z_0$ , or static probe height above the relaxed surface. We control  $w$  by simply changing the scanning feedback set-point at regular intervals along the slow scan axis (see Fig. 3(c)). Figure 6 shows an example of the measured and simulated force quadratures for the Tap525 cantilever at three different probe heights. All simulation curves shown in the figure used the same parameters given in Table I, changing only the working distance  $w$  which is given in Fig. 6. Equivalent plots for the NSC15 and AC55 cantilevers are shown in the supplemental ma-

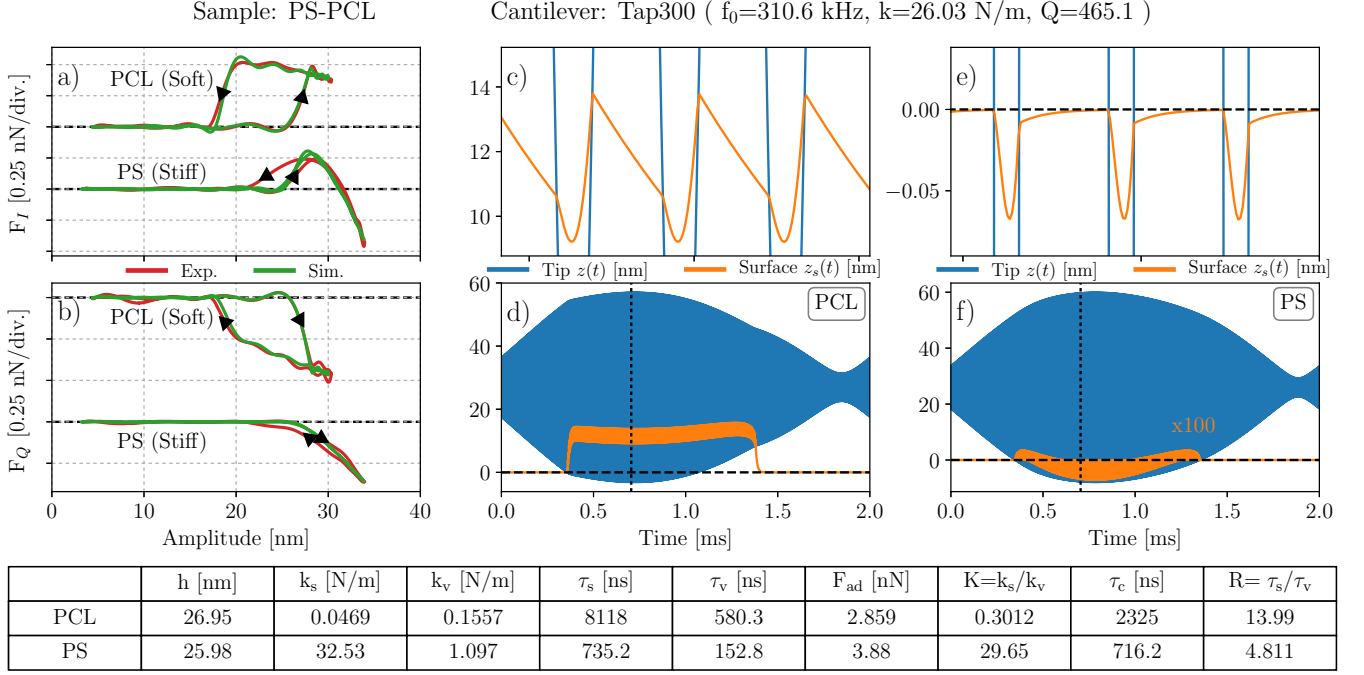


FIG. 4. **Polystyrene/polycaprolactone blend.** (a) The conservative force quadrature  $F_T(A)$  and (b) the dissipative quadrature  $F_Q(A)$ . The curves are offset vertically for clarity with dashed lines corresponding to zero force. The simulated motion of the tip  $z(t)$  (blue) and surface  $z_s(t)$  (orange) are shown for both PCL (c) and (d) and PS [(e) and (f)]. The zooms (c) and (e) showing details of the surface motion around the time marked by the vertical dotted line in (d) and (f) respectively. The surface motion of PS in (f) is magnified by a factor of 100. Note that the average surface position for PCL is  $\sim 12$  nm above its rest position, while PS deviates only  $\sim 0.05$  nm from its equilibrium position. The best-fit parameters used in simulation are given in the table.

terial Figs. S1 and S2 respectively.

To further test the model we also analyzed a nanoparticle membrane sample shown in Fig. 3(d). This sample consists of a monolayer of Au nanoparticles, bound together by organic ligands. The membrane is suspended over a circular hole  $2.5\mu\text{m}$  in diameter, forming an ultra-thin drum head [38, 39]. Previous studies have shown large apparent stiffness, corresponding to a large effective bulk modulus of the membrane material [40]. Interpretation of the model parameter  $k_v$  in terms of bulk compression is not obvious with these samples that have thickness  $\simeq 7\text{nm}$ . However, adhesion gives rise to very large curvature of upper and lower surfaces of the membrane as it covers the tip with very small radius. The Laplace pressure change across both of these interfaces will add, giving the force described by  $k_v$  which acts in opposition to adhesion. The stiffness constant  $k_s$  would then describe elastic tension in the membrane as the surface deviates from equilibrium. It is therefore not surprising that our simple model fits the data quite well. Figure 7 shows a comparison of experiment and simulation of the model for two different cantilevers. The qualitative shape of the force quadratures and the simulated dynamics of the surface are the same for both cantilevers, despite the difference in resonance frequency of AC55 ( $\sim 2$  MHz) and Tap300 ( $\sim 300$  kHz).

#### IV. DISCUSSION

An obvious criticism of the model presented herein is that it is *ad hoc*, or not based on first principles. Nonlinear forces arising from sample deformation, the analysis of which forms the basis of traditional AFM nanomechanics, are avoided by linear approximation. The model keeps only one nonlinearity to capture the sudden impact and release of the tip and sample. Reduction of the sample dynamics to one effective degree of freedom  $d_s(t)$  is a sweeping simplification which neglects the fact that the surface deformation has a transverse profile. We emphasize again that our intent is to describe the measured dynamics of the cantilever with a minimum number of free parameters and additional degrees of freedom. We consider this to be the minimal model necessary for explaining dynamic AFM on viscoelastic materials, and in our experience it is often sufficient.

Starting from first principles, even very idealized models would involve many parameters: tip radius and side-wall angle - assuming an axial-symmetric tip; elastic modulus, Poisson ratio and viscosity - assuming an infinite homogeneous half-space; surface energies and local curvature of the unperturbed surface. All of these parameters which are not independently determined, must be treated as free when fitting AFM data. The fit proce-



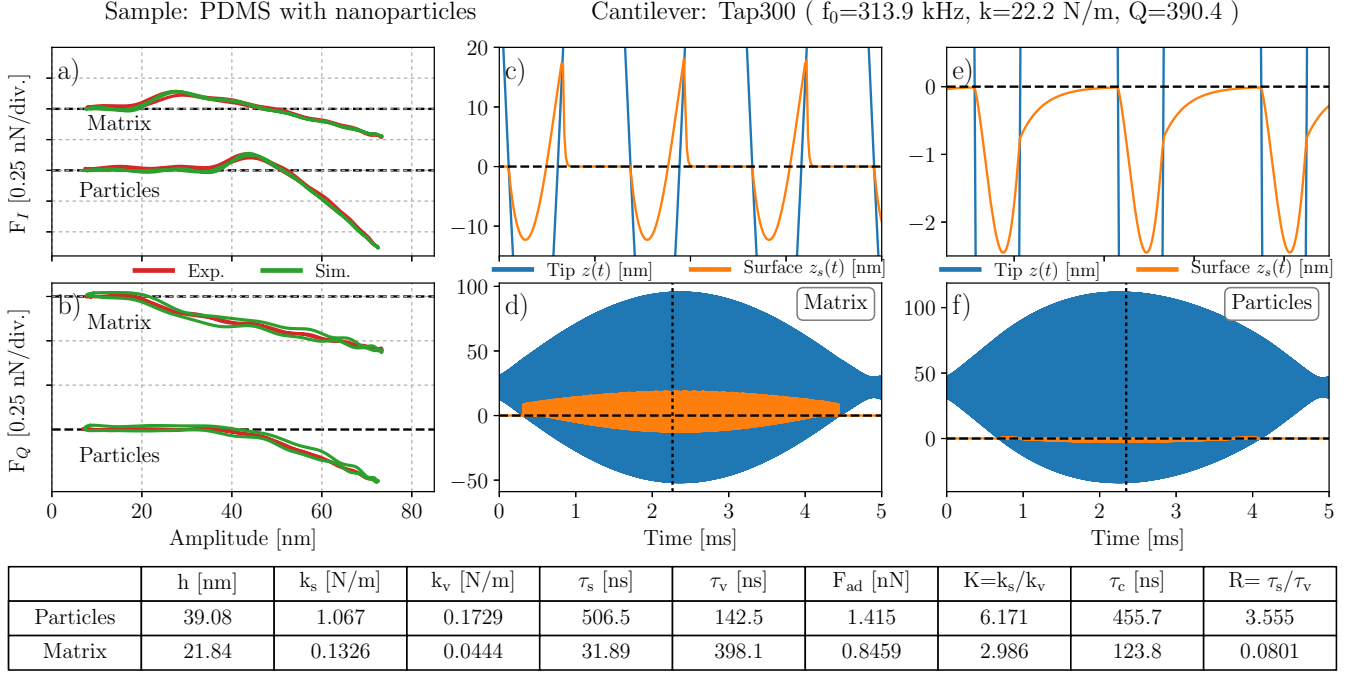


FIG. 5. **PDMS with hydrophobic silica nanoparticles.** The details of this sample are described in a previous publication [36]. The curves labeled Matrix were measured on the softer PDMS, where the simulation shows large amplitude surface motion and deep tip penetration. The curves labeled Particles were measured on a subsurface aggregation of nanoparticles, where the simulation reveals very little surface motion and lifting, yet equally deep tip penetration. (a) The conservative force quadrature  $F_I(A)$  and (b) the dissipative quadrature  $F_Q(A)$ . The curves are offset vertically for clarity with dashed lines corresponding to zero force. The simulated motion of the tip  $z(t)$  (blue) and surface  $z_s(t)$  (orange) are shown for both the PDMS matrix (c) and (d) and a cluster of particles (e) and (f). The zooms (c) and (e) showing details of the surface motion around the time marked by the vertical dotted line in (d) and (f) respectively. The best-fit parameters used in the simulation are given in the table.

dure here uses the multifrequency ImAFM data at some 40 frequencies near resonance. While the quadrature data (80 values) do have different weight (they are measured with different signal-to-noise ratio) each represents an independent observable with information about the tip-sample interaction. The rather large number of measured data in relation to the number of free parameters in our minimal model makes physical interpretation of the fitted parameter values meaningful.

Examining Table I, we recall that the cantilever parameters  $f_0$ ,  $Q$  and  $k$  are independently calibrated (see Methods), and the working distance  $w$  can be determined by inspection (amplitude at the initial sharp rise in  $F_I$ ). Thus the 5 parameters  $F_{ad}$ ,  $k_s$ ,  $\eta_s$ ,  $k_v$ ,  $\eta_v$ , are free parameters. We expect that all of these will depend on the detailed shape of the tip. It is therefore not so surprising that the table shows considerable variation of these parameters between the different probes. We might however expect that the relaxation times  $\tau_{s(v)} = \frac{\eta_{s(v)}}{k_{s(v)}}$  would be less sensitive to tip shape. For example, a blunt tip should result in both larger viscous and large elastic force, in comparison with a sharper tip. The ratio of these force constants might therefore be independent of the sharpness of the tip. Indeed, we do observe less variation in

the values of  $\tau_{s(v)}$ .

It is interesting to note in Table I and in the table of Fig. 7, that the ratio of time constants

$$R = \frac{\tau_s}{\tau_v} = \frac{\eta_s k_v}{k_s \eta_v} \quad (12)$$

is apparently independent of the AFM probe used in the experiment. We call  $R$  the impact-rheology factor [41], a dimensionless number formed from all four force constants of our linear viscoelastic model. Our measurements suggests that this factor may be a good quantity for physical characterization of surface viscoelasticity.

It is difficult to quantify measurement uncertainty in  $R$ , as this depends on how various sources of noise in the experiment propagate to the model parameters when fitting to our highly nonlinear model. Further experimental studies and more detailed model analysis are required to study uncertainties, and verify if the impact-rheology factor is indeed a reliable measurement of an intrinsic property of the sample interface.

While this moving surface model is minimal with regard to the number of parameters, it nevertheless has very complicated dynamics. General statements about its behavior in different parameter regimes are therefore

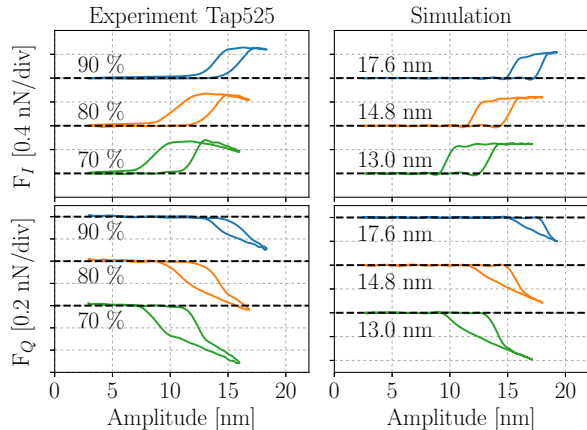


FIG. 6. **Low-density polyethelene (LDPE) with Tap525 cantilever.** Experimental (left) and simulated (right) force quadrature curves, each offset vertically for clarity with dashed lines corresponding to zero force. The experimental curves result from analysis of data at pixels marked with an  $\times$  of the corresponding color in Fig. 3(c). The working distance was changed in the experiment by adjusting the amplitude-feedback setpoint to the value given in left panels (% of free amplitude). For simulation the working distance  $w$  shown in the right panels was found by numerical optimization with all other parameters of the model fixed at the values given in Table I.

Cantilever	NSC15	Tap525	AC55
$f_0$ [kHz]	230	489	2120
$Q$	397	547	735
$k$ [N/m]	18.9	88.6	161
$A_{\text{free}}$ [nm]	20	11	6.3
$F_{\text{ad}}$ [nN]	0.955	1.8	0.818
$k_s$ [N/m]	0.17	0.858	0.227
$\eta_s$ [kg/s]	$3.01 \cdot 10^{-6}$	$14.9 \cdot 10^{-6}$	$2.75 \cdot 10^{-6}$
$\tau_s$ [ $\mu$ s]	17.68	17.31	12.11
$k_v$ [N/m]	0.04	0.0238	0.014
$\eta_v$ [kg/s]	$8.24 \cdot 10^{-8}$	$4.74 \cdot 10^{-8}$	$1.92 \cdot 10^{-8}$
$\tau_v$ [ $\mu$ s]	2.06	1.99	1.37
$K$	4.25	3.6	16.21
$\tau_c$ [ $\mu$ s]	14.7	17.1	11.5
$R$	8.61	8.69	8.86

TABLE I. **Simulation parameters for LDPE for three different cantilevers.** The calibrated cantilever parameters and fitted model parameters. Various ratios of the fitted parameters are: the relaxation times  $\tau_s = \eta_s/k_s$  and  $\tau_v = \eta_v/k_v$ , the stiffness ratio  $K = k_s/k_v$ , contact formation time  $\tau_c = (\eta_s + \eta_v)/(k_s + k_v)$  and impact-rheology factor  $R = \tau_s/\tau_v$ . Although the stiffness and damping constants differ between probes, the relaxation times and impact-rheology factor are remarkably similar for all cantilevers.

difficult to formulate. The impact-rheology factor represents the relative strength of two viscoelastic processes: large  $R$  means that the samples free relaxation to equilibrium in the absence of the tip, is slow in comparison to the time needed to locally deform the sample and accommodate the penetrating tip. Conversely, small  $R$  means that tip penetration is slow in comparison with free relaxation. However, the magnitude of  $R$  alone is insufficient to predict the shape of the force quadrature curves, which also depend on the adhesion force, working distance, and frequency of oscillation. Hysteresis is associated with  $\omega_0\tau_s \gg 1$ , large surface lifting with small  $k_s$  or large  $\delta_0$ , and deep penetration with small  $k_v$ .

## V. CONCLUSIONS

We presented a minimal model for dynamic AFM on viscoelastic materials, accounting for both surface and bulk forces. The model is simple in that it is linear where possible, but its dynamics is complex due to the nonlinearity describing the sudden impact and release of the oscillating tip and surface. Unlike traditional nanomechanical analysis of AFM, our model takes in to account the viscoelastic dynamics of both the tip and the sample. The sample dynamics was shown to be quite significant on soft materials, where simulations revealed large amplitude surface motion. We validated the model by showing excellent agreement with experimental data on a variety of samples. Fitting the model to the data we extracted viscous and elastic force constants for the surface and bulk. Our analysis indicated that the impact-rheology factor, formed from the dimensionless ratio of these constants, is independent of tip shape and probe frequency. The models explanation of numerous measured force quadrature curves with complex and differing shape, instills confidence in its ability to describe the essential physics of dynamic AFM on soft materials.



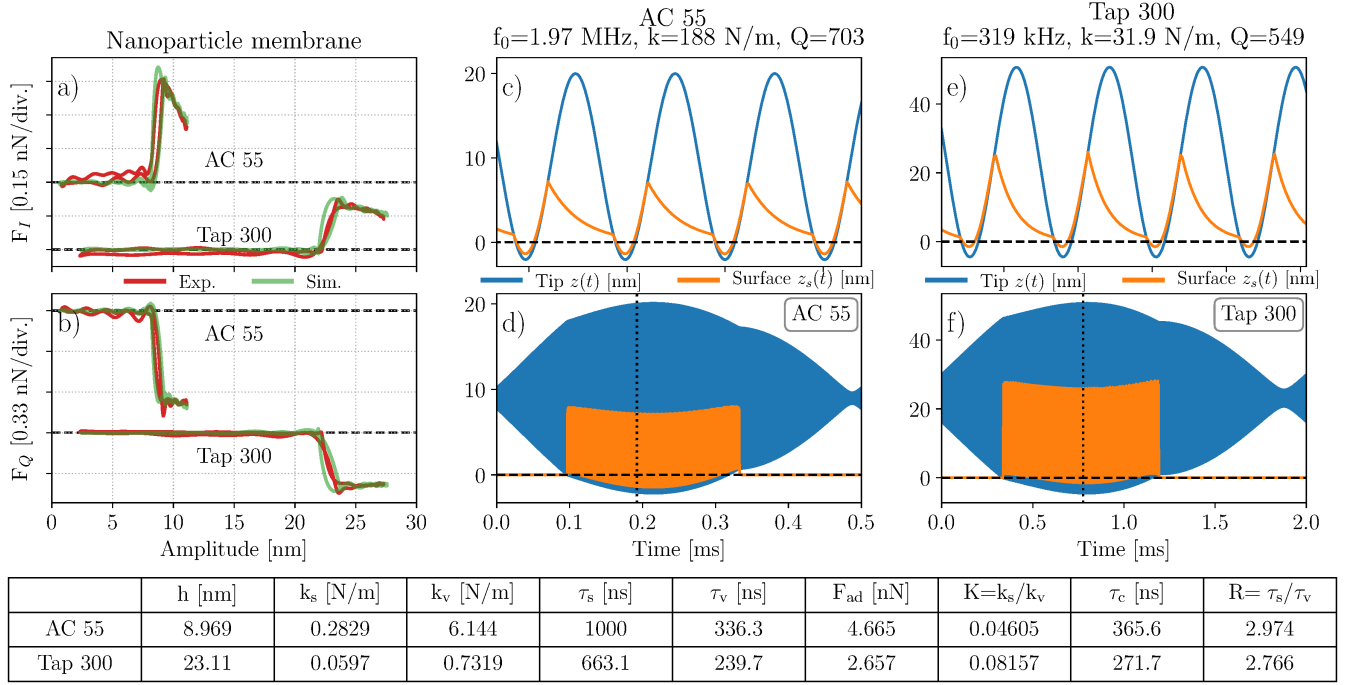


**FIG. 7. Nanoparticle membrane with Tap300 and AC55.** Measurements were made in the middle of a membrane with diameter  $2.5\mu\text{m}$ . We show results from two different membranes from the same batch, measured with two different cantilevers. **(a)** The conservative force quadrature  $F_I(A)$  and **(b)** the dissipative quadrature  $F_Q(A)$ . The curves are offset vertically for clarity with dashed lines corresponding to zero force. **(c)** and **(d)** show the simulated motion of the tip  $z(t)$  (blue) and surface  $z_s(t)$  (orange) for cantilever AC55, and **(e)** and **(f)** for cantilever Tap300. The zooms **(c)** and **(e)** show details of the surface motion around the time marked by the vertical dotted line in **(d)** and **(f)** respectively. The best-fit parameters used in the simulation are given in the table.

## Appendix: Methods

### 1. Equations of motion

For numerical simulation of the tip and surface motion it is convenient to introduce a non-dimensional time  $u = 2\pi f_0 t$ , where  $f_0$  is the resonant frequency of the cantilever in Hz. This scaling allow us to express the relaxation times as dimensionless parameters,  $u_s = \omega_0 \tau_s$  and  $u_v = \omega_0 \tau_v$ . Equations (2a) and (2b) then describe a three-dimensional dynamical system with state variables  $d$ ,  $d'$  and  $d_s$ . For the case  $s < 0$  this system reads,

$$\frac{d}{du}d = d' \quad (\text{A.1a})$$

$$\begin{aligned} \frac{d}{du}d' = & -\frac{1}{Q}d' - d + \frac{F_d}{k} - \frac{F_{ad}}{k} \\ & - \frac{k_v}{k}(s + u_v s') \end{aligned} \quad (\text{A.1b})$$

$$\begin{aligned} \frac{d}{du}d_s = & d'_s = -\frac{d_s}{u_s} + \frac{k_v}{u_s k_s} \\ & \times \left( \frac{F_{ad}}{k_v} + s + u_v(d' - d'_s) \right) \end{aligned} \quad (\text{A.1c})$$

Since the right hand side of eq. (A.1b) depends on  $s' = d' - d'_s$ , we must first solve eq. (A.1c) for  $d'_s$  and then substitute it in to the right hand side of eq. (A.1b). In terms of the impact-rheology factor  $R = \frac{u_s}{u_v}$  and the stiffness ratio  $K = k_s/k_v$  we can write this system as:

$$\frac{d}{du}d = d' \quad (\text{A.2a})$$

$$\begin{aligned} \frac{d}{du}d_s = & \frac{1}{1 + RK} \left( -\frac{d_s}{u_s} + \frac{1}{u_s K} \right. \\ & \times \left. \left( \frac{F_{ad}}{k_v} + s + u_v d' \right) \right) \end{aligned} \quad (\text{A.2b})$$

$$\begin{aligned} \frac{d}{du}d' = & -\frac{1}{Q}d' - d + \frac{F_d}{k} - \frac{F_{ad}}{k} \\ & - \frac{k_v}{k}(s + u_v s') \end{aligned} \quad (\text{A.2c})$$

The prefactor  $\frac{1}{1+RK}$  in front of eq. (A.2b) describes the strength of the dynamic coupling between tip and surface, giving a measure of how much surface motion one can expect.

### 2. Numerical integration and optimization

Numerical integration of the model is performed with the package CVODE, part of the SUNDIALS suite of nonlinear solvers [42]. This integrator has adaptive time-stepping and so-called 'discrete event detection' which allows for accurate treatment of the discontinuity in force occurring at the point of contact  $s = 0$ . Because the dynamical system is coded in C, simulation time is reduced

by a factor of 100 in comparison with coding in higher-level languages such as *MATLAB* or *Python*. This speed up is of great importance as many integrations are required when iterating to find the optimal parameters. The initial conditions for  $d$  and  $d'$  are reset to their measured values for each integration, whereas the initial condition for  $d_s$  is set to zero on the first integration, and then estimated from the previous integration for all subsequent integrations.

The free model parameters are found through numerical optimization. We used the Python library *scipy.optimize.leastsq*, which is a wrapper for MINPACK's implementation of the Levenberg-Marquardt algorithm. The algorithm performs a least-square minimization of the array of residuals  $r = \{\text{real}(\hat{F}_{exp} - \hat{F}_{sim}), \text{imag}(\hat{F}_{exp} - \hat{F}_{sim})\}$  where the  $\hat{F}(\omega)$  are experimental and simulated complex force amplitudes at 40 frequencies. The method finds a local minimum, starting from good initial parameter values determined by trial and error.

Each measurement (one pixel of the scan) required 2 ms, corresponding to a frequency spacing in the comb of intermodulation products of 500 Hz, also the measurement bandwidth. To enhance the signal-to-noise ratio, we average the measured intermodulation spectra over several neighboring pixels which show the same type of response, thereby using spatial correlation to reduce the noise. This averaging results in smoother experimental force quadrature curves without reducing the scan speed.

### 3. Background force compensation

When the cantilever is oscillating above a surface we often observe significant background forces, not resulting from tip-sample interaction force but rather acting over the entire cantilever body. The origin of these background forces might be *e.g.* long-range electrostatic force or hydrodynamic squeeze-film damping. In order to deduce the tip-sample force we need to remove this background interaction. The procedure we use for removing any linear background force is described in a previous publication [43].

### 4. Calibration

Cantilever parameters are determined by the non-invasive thermal calibration method described by Higgins *et al.* [44], which combines the fluctuation dissipation theorem with Sader's method based on analysis of hydrodynamic damping [45]. With this approach one can extract the three parameters of the cantilever transfer function,  $k$ ,  $f_0$  and  $Q$ , as well as the inverse responsivity of the optical detector used to measure cantilever deflection  $\alpha^{-1}[\text{nm/V}]$ , all from one measurement of the thermal Brownian motion of the cantilever near resonance. The method is encapsulated in the recently launched Global

Calibration Initiative (GCI) [46], where a thermal noise measurement of  $f_0$  and  $Q$  can be used to get  $k$ , based on a single hydrodynamic constant determined from averaging over the measurements of many users on the same type of cantilever. We took our measured  $f_0$  and  $Q$  and used the GCI to determine  $k_{\text{Sader}}$ , allowing us to then determine  $\alpha^{-1}$ . Note that error in the calibration of  $k$  and  $\alpha^{-1}$  result in a re-scaling of the force and amplitude axes respectively, which does not change the general shape of the force quadrature curves.

## ACKNOWLEDGMENTS

We acknowledge S. Borysov, C. A. van Edysen, J. Wettlaufer and Xiao-min Lin for helpful discussions, and J. Jureller for help with the measurements. KTH authors are grateful for financial support from the Swedish Research Council (VR), the Olle Engkvist Foundation and the Knut and Alice Wallenberg Foundation. Ph.L. is FRS-FNRS Senior Research Associate. Research in Mons was supported by the European Commission and Region Wallonne FEDER program, the Science Policy Office of the Belgian Federal Government (BELSPO-PAI VII/5), and the FRS-FNRS PDR Project ECOSTOFLEX. Y.W. and H.M.J. acknowledge support from the Office of Naval Research through grant N00014-17-1-2342 and through the Chicago MRSEC under NSF DMR-1420709.

- 
- [1] A. Yango, J. Schape, C. Rianna, H. Doschke, and M. Radmacher, *Soft Matter* **12**, 8297 (2016).
  - [2] Y. M. Efremov, W.-H. Wang, S. D. Hardy, R. L. Geahlen, and A. Raman, *Scientific Reports* **7**, 1541 (2017).
  - [3] F. M. Hecht, J. Rheinlaender, N. Schierbaum, W. H. Goldmann, B. Fabry, and T. E. Schaffer, *Soft Matter* **11**, 4584 (2015).
  - [4] B. K. Connizzo and A. J. Grodzinsky, *Journal of Biomechanics* **54**, 11 (2017).
  - [5] D. C. Hurley and J. P. Killgore, "Dynamic contact afm methods for nanomechanical properties," in *Scanning Probe Microscopy in Industrial Applications* (John Wiley & Sons, Inc, 2013) pp. 115–149.
  - [6] G. Stan and R. S. Gates, *Nanotechnology* **25**, 245702 (2014).
  - [7] I. Chakraborty and D. G. Yablon, *Polymer* **55**, 1609 (2014).
  - [8] M. Chyasnachyus, S. L. Young, and V. V. Tsukruk, *Japanese Journal of Applied Physics* **54**, 08LA02 (2015).
  - [9] H. K. Nguyen, M. Ito, and K. Nakajima, *Japanese Journal of Applied Physics* **55**, 08NB06 (2016).
  - [10] E. Rezaei and J. A. Turner, *Applied Physics Letters* **110**, 101902 (2017), <http://dx.doi.org/10.1063/1.4977936>.
  - [11] P. M. Claesson, I. Dobryden, G. Li, Y. He, H. Huang, P.-A. Thoren, and D. B. Haviland, *Phys. Chem. Chem. Phys.* **19**, 23642 (2017).
  - [12] A. Maali, R. Boisgard, H. Chraïbi, Z. Zhang, H. Kellay, and A. Würger, *Phys. Rev. Lett.* **118**, 084501 (2017).
  - [13] A. B. Churnside, R. C. Tung, and J. P. Killgore, *Langmuir* **31**, 11143 (2015), pMID: 26426705, <http://dx.doi.org/10.1021/acs.langmuir.5b02860>.
  - [14] H. Schlicke, E. W. Leib, A. Petrov, J. H. Schröder, and T. Vossmeier, *The Journal of Physical Chemistry C* **118**, 4386 (2014), <http://dx.doi.org/10.1021/jp4091969>.
  - [15] T. Ando, T. Uchihashi, and N. Kodera, *Annual Review of Biophysics* **42**, 393 (2013), pMID: 23541159, <https://doi.org/10.1146/annurev-biophys-083012-130324>.
  - [16] B. P. Brown, L. Picco, M. J. Miles, and C. F. J. Faul, *Small* **9**, 3201 (2013).
  - [17] C. A. Amo, A. P. Perrino, A. F. Payam, and R. Garcia, *ACS Nano* (2017), 10.1021/acsnano.7b04381, pMID: 28770996, <http://dx.doi.org/10.1021/acsnano.7b04381>.
  - [18] A. X. Cartagena-Rivera, W.-H. Wang, R. L. Geahlen, and A. Raman, **5**, 11692 (2015).
  - [19] R. Miller, J. K. Ferri, A. Javadi, J. Krägel, N. Mucic, and R. Wüstneck, *Colloid and Polymer Science* **288**, 937 (2010).
  - [20] F. Peterka, "Dynamics of the impact oscillator," in *IUTAM Symposium on New Applications of Nonlinear and Chaotic Dynamics in Mechanics: Proceedings of the IUTAM Symposium held in Ithaca, NY, U.S.A., 27 July–1 August 1997*, edited by F. C. Moon (Springer Netherlands, Dordrecht, 1999) pp. 283–292.
  - [21] D. Platz, E. A. Tholen, D. Pesen, and D. B. Haviland, *Appl. Phys. Lett.* **92**, 153106 (2008).
  - [22] H. Hertz, *Journal für die reine und angewandte Mathematik* **92**, 156 (1881).
  - [23] A. He and J. S. Wettlaufer, *Soft Matter* **10**, 2264 (2014).
  - [24] S. D. Solares, *Beilstein J. Nanotechnol.* **7**, 554 (2016).
  - [25] P. Attard, *Journal of Physics: Condensed Matter* **19**, 473201 (2007).
  - [26] P. de Gennes, F. Brochard-Wyart, and D. Quere, *Capillarity and Wetting Phenomena: Drops, Bubbles, Pearls, Waves* (Springer, 2004).
  - [27] K. L. Johnson, K. Kendall, and A. D. Roberts, *Proceedings of the Royal Society of London. Series A, Mathematical and Physical Sciences* **324**, 301 (1971).
  - [28] R. W. Style, C. Hyland, R. Boltyanskiy, J. S. Wettlaufer, and E. R. Dufresne, *Nature Communications* **4**, 2728 EP (2013).
  - [29] H.-J. Butt, J. T. Pham, and M. Kappl, *Current Opinion in Colloid & Interface Science* **27**, 82 (2017).
  - [30] J. H. Cantrell and S. A. Cantrell, "Cantilever dynamics: Theoretical modeling," in *Acoustic Scanning Probe Microscopy*, edited by F. Marinello, D. Passeri, and E. Savio (Springer Berlin Heidelberg, Berlin, Heidelberg, 2013) pp. 47–100.
  - [31] D. B. Haviland, C. A. van Edysen, D. Forchheimer, D. Platz, H. G. Kassa, and P. Leclerc, *Soft Matter* **12**, 619 (2016).
  - [32] J. Melcher, S. Hu, and A. Raman, *Review of Scientific Instruments* **79**, 061301 (2008).

- [33] D. Platz, D. Forchheimer, E. A. Tholén, and D. B. Haviland, *Nanotechnology* **23**, 265705 (2012).
- [34] D. Platz, D. Forchheimer, E. A. Tholén, and D. B. Haviland, *Nat Commun* **4**, 1360 (2013).
- [35] D. B. Haviland, *Current Opinion in Colloid & Interface Science* **27**, 74 (2017).
- [36] H. Huang, I. Dobryden, P.-A. Thorén, L. Ejenstam, J. Pan, M. Fielden, D. Haviland, and P. Claesson, *Composites Science and Technology* **150**, 111 (2017).
- [37] “Harmonix test sample, bruker corp.”.
- [38] J. He, P. Kanjanaboos, N. L. Frazer, A. Weis, X.-M. Lin, and H. M. Jaeger, *Small* **6**, 1449 (2010).
- [39] P. Kanjanaboos, X.-M. Lin, J. E. Sader, S. M. Rupich, H. M. Jaeger, and J. R. Guest, *Nano Letters* **13**, 2158 (2013), pMID: 23614346, <http://dx.doi.org/10.1021/nl401230z>.
- [40] Y. Wang, H. Chan, B. Narayanan, S. P. McBride, S. K. R. S. Sankaranarayanan, X.-M. Lin, and H. M. Jaeger, *ACS Nano* **11**, 8026 (2017), pMID: 28715195, <http://dx.doi.org/10.1021/acsnano.7b02676>.
- [41] “Not to be confused with the rheology impact factor,”.
- [42] A. C. Hindmarsh, P. N. Brown, K. E. Grant, S. L. Lee, R. Serban, D. E. Shumaker, and C. S. W. ACM, *Transactions on Mathematical Software* **31**, 363 (2005).
- [43] R. Borgani, P.-A. Thorén, D. Forchheimer, I. Dobryden, S. M. Sah, P. M. Claesson, and D. B. Haviland, *Phys. Rev. Applied* **7**, 064018 (2017).
- [44] M. J. Higgins, R. Proksch, J. E. Sader, M. Polcik, S. M. Endoo, J. P. Cleveland, and S. P. Jarvis, *Review of Scientific Instruments* **77**, 013701 (2006).
- [45] J. E. Sader, J. A. Sanelli, B. D. Adamson, J. P. Monty, X. Wei, S. A. Crawford, J. R. Friend, I. Marusic, P. Mulvaney, and E. J. Bieske, *Review of Scientific Instruments* **83**, 103705 (2012).
- [46] J. E. Sader, R. Borgani, C. T. Gibson, D. B. Haviland, M. J. Higgins, J. I. Kilpatrick, J. Lu, P. Mulvaney, C. J. Shearer, A. D. Slattery, P.-A. Thorén, J. Tran, H. Zhang, H. Zhang, and T. Zheng, *Review of Scientific Instruments* **87**, 093711 (2016), <http://dx.doi.org/10.1063/1.4962866>.